TSpace Research Repository tspace.library.utoronto.ca

2D matrix engineering for homogeneous quantum dot coupling in photovoltaic solids

Jixian Xu, Oleksandr Voznyy, Mengxia Liu, Ahmad R. Kirmani, Grant Walters, Rahim Munir, Maged Abdelsamie, Andrew H. Proppe, Amrita Sarkar, F. Pelayo García de Arquer, Mingyang Wei, Bin Sun, Min Liu, Olivier Ouellette, Rafael Quintero-Bermudez, Jie Li, James Fan, Lina Quan, Petar Todorovic, Hairen Tan, Sjoerd Hoogland, Shana O. Kelley, Morgan Stefik, Aram Amassian & Edward H. Sargent

Version Post-print/accepted manuscript

Citation (published version) Xu, Jixian, Oleksandr Voznyy, Mengxia Liu, Ahmad R. Kirmani, Grant Walters, Rahim Munir, Maged Abdelsamie et al. "2D matrix engineering for homogeneous quantum dot coupling in photovoltaic solids." Nature nanotechnology(2018): 1. Doi: 10.1038/s41565-018-0117-z

How to cite TSpace items

Always cite the published version, so the author(s) will receive recognition through services that track citation counts, e.g. Scopus. If you need to cite the page number of the **author manuscript from TSpace** because you cannot access the published version, then cite the TSpace version **in addition to** the published version using the permanent URI (handle) found on the record page.

This article was made openly accessible by U of T Faculty. Please tell us how this access benefits you. Your story matters.

UNIVERSITY OF TORONTO LIBRARIES

2D matrix engineering for homogeneous quantum dot coupling in photovoltaic solids

Jixian Xu[1], Oleksandr Voznyy[1], Mengxia Liu[1], Ahmad R. Kirmani[2], Grant Walters[1], Rahim Munir[2], Maged Abdelsamie[2], Andrew H. Proppe[1], Amrita Sarkar[3], F. Pelayo García de Arquer[1], Mingyang Wei[1], Bin Sun[1], Min Liu[1,4], Olivier Ouellette[1], Rafael Quintero-Bermudez[1], Jie Li[1], James Fan[1], Lina Quan[1], Petar Todorovic[1], Hairen Tan[1], Sjoerd Hoogland[1], Shana O. Kelley[5], Morgan Stefik[3], Aram Amassian[2*] and Edward H. Sargent[1*]

[1]*Department of Electrical and Computer Engineering, University of Toronto, 35 St George Street, Toronto, Ontario M5S 1A4, Canada*

[2]*King Abdullah University of Science and Technology (KAUST), KAUST Solar Center (KSC), and Physical Sciences and Engineering Division, 4700 KAUST, Thuwal 23955-6900, Saudi Arabia*

[3]*Department* of Chemistry and *Biochemistry, University of South Carolina, Columbia, South Carolina 29208, USA*

[4]*Institute of Super-microstructure and Ultrafast Process in Advanced Materials, School of Physics and Electronics, Central South University, 932 South Lushan Road, Changsha, Hunan 410083, P. R. China*

[5]*Department of Pharmaceutical Sciences, Leslie Dan Faculty of Pharmacy, University of Toronto, Toronto, Ontario M5S 3M2, Canada*

*Correspondence and requests for materials should be addressed to Aram Amassian (aram.amassian@kaust.edu.sa) and Edward H. Sargent (ted.sargent@utoronto.ca) (E.H.S)

Colloidal quantum dots (CQDs) are promising photovoltaic materials in view of their widely tunable absorption spectrum controlled by nanocrystal size[1,2]. Their bandgap tunability allows not only the optimization of single-junction cells, but also the fabrication of multi-junction cells that complement perovskites and silicon[3]. Advances in surface passivation[2,4–7], combined with advances in device structures[8], have contributed to certified power conversion efficiencies (PCEs) that rose to 11% in 2016[9]. Further gains in performance are available if the thickness of the devices can be increased to maximize light harvesting at high fill factor. However, the active layer thickness is limited today to ~300 nm by the concomitant photocarrier diffusion length. To date, CQD devices thicker than this typically exhibit decreases in short-circuit current (JSC) and open-circuit voltage (VOC), as seen in previous reports[3,9–11]. Here we report a matrix engineering strategy for CQD solids that significantly enhances the photocarrier diffusion length. We find that a hybrid inorganic:amine coordinating complex enables us to generate a high-quality 2D-confined inorganic

matrix that programs inter-nanoparticle spacing at the atomic scale. This strategy enables the reduction of structural and energetic disorder in the solid and concurrent improvements in CQD packing density and uniformity. Consequently, planar devices with nearly doubled active layer thicknesses (~600 nm) and record values of short-circuit current (32 mA cm^{-2}) are fabricated. The open-circuit voltage was improved at the same time as current was increased. We demonstrate CQD solar cells with a certified record efficiency of 12%.

In recent studies, composition-matching matrices have been explored as a solder between CQDs to improve carrier mobility[12]. Lattice-matching matrices such as perovskites have been shown to improve the efficiency of CQD luminescence[13]. We reasoned that the limited photocarrier diffusion length and V_{OC} deficit could arise from spatial variations in the nanostructure of the matrix throughout a CQD PV film (Fig.1). Photocarrier transport between CQDs is sensitive to the thickness of the interstitial matrix, at the atomic scale, from the perspective both of electronic tunneling and of resonance energy transfer[1,12–15]. Detrimental inhomogeneity in the matrix (such as CQD over-coupling due to surface fusion in the absence of matrix; or CQD over-isolation due to matrix accumulations) increases structural and energetic disorder and degrades the diffusion length in the film as well as the devices' V_{OC} (Fig. 1d) [3,10,14–17].

Rutherford backscattering spectroscopy (RBS) studies of previously-reported best-performing PbS CQD PV solids[9] reveal a matrix component that includes stoichiometric PbI_2 in surprisingly high amounts: 40 ~ 50 % relative to PbS (Fig. 1b and Supplementary Fig. 1). This agrees with the amount required for full monolayer coverage on the surfaces of the PbS CQDs (bandgap ~1.3eV and diameter ~3 nm). We believed that the conditions under which such matrices are formed during film solidification could benefit from further attention.

We pursued therefore the goal of increasing the photocarrier diffusion length in CQD PV solids via matrix improvements (Fig. 1c and 1e). We would do so by limiting the PbI_2 matrix component to be a two-dimensional material, a strategy enabled by developing a PbI_2-hybrid-amine coordinating complex that forms in a manner analogous to the materials synthesis of 2D perovskites[18,19] (Fig. 1c). The strategy

promotes the growth of the PbI_2 matrix into a single-atomically-thin layered configuration. We sought the 2D strategy to prevent the formation of thick (multiple atomic layers) regions of matrix that could otherwise form during film solidification.

We investigated PbI_2-hybrid-amine coordinating complexes initially using UV-Vis-NIR absorption spectroscopy (Fig. 2a). We compared PbI_2 films prepared from dimethylformamide (DMF, the aprotic polar solvent used for CQD solution-exchange), pure butylamine (BTA, control solvent used in the best previously published CQD PVs[9]) and the hybrid-amine mixtures (butylamine and hexylamine; see Methods for details). A strong excitonic absorption peak ($\lambda \sim 500$ nm) was found in the hybrid-amine PbI_2 films. This feature was much less significant in the BTA case (Supplementary Fig. 2) and was not detectable in the DMF case. We associate the excitonic feature with quantum confined layered structures observed in previous studies: layered 2D PbI_2-organic hybrid perovskites[18,19]. This notion is further confirmed by photoluminescence (PL) studies (Fig. 2b). The sharp and asymmetric PL emission (peak $\lambda \sim$ 520 nm, full-width at half-maximum ~16 nm) of hybrid-amine films is a signature of the independent and substantially homogeneous population of PbI_2 monolayers. Such PL features have typically been observed in layered 2D perovskite single crystals[18] and layered PbI_2 single crystals under cryogenic conditions[20]. The emission spectra for BTA films are much broader and darker (Supplementary Fig. 2). We ascribe this to the presence of less self-similar, and/or less confined, layered structures. In contrast, the random 3D growth habit of DMF films yields negligible emission, due to the numerous defects at grain surfaces and the mutual quenching effect[20,21].

We noticed that the PL linewidth (~ 16 nm) of PbI_2-hybrid-amine films is comparable to that in 2D perovskite single crystals (~16 nm) and is superior to that in 2D perovskite films (> 40 nm, Supplementary Fig. 3). This near-single-crystalline feature motivated crystallography measurements that employed grazing incidence wide-angle X-ray scattering (GIWAXS). Conventional DMF films exhibited no detectable layered features (Fig. 2c). By contrast, sharp and discrete Bragg spots along the q_z axis are

observed in hybrid-amine films (Fig. 2d and Supplementary Fig. 4), revealing a high-quality 2D monolayer structure with long-range ordering and orientation. This finding indicated the potential to enhance 2D confinement of the PbI_2 matrix component by leveraging the hybrid-amine coordination.

We used Fourier transform infrared spectroscopy (FTIR) to gain a further mechanistic understanding of the PbI_2-amine complex in CQD films (Fig. 2c). First, the coordination effect of amines on PbI_2 is confirmed by the consistent shift of the N-H stretch mode (3170 cm^{-1}) and N-H scissor mode (1560 cm^{-1}) in PbI_2-amine complexes compared with those in reference solvents of amines (Supplementary Fig. 4)[22]. This signature of 2D PbI_2-amine complexes is present identically both in PbI_2 films and PbI_2-capped CQD films prepared using amines (Fig. 2e and Supplementary Fig. 5 and 6c). Moreover, when the matrix-to-CQD ratio is tuned, the spectral signature of the 2D PbI_2-amine complex in CQD films is retained in FTIR measurements (Supplementary Fig. 7d); and its lattice pattern is also identified using GIWAXS (Supplementary Fig. 7b). In contrast, such features are absent both in PbI_2 films and CQD films prepared using DMF (Fig. 2e and Supplementary Fig. 6f and 7h). This comparison indicates that the CQD surface functionalization mechanism is inherited from the PbI_2-amine 2D coordination in the matrix, rather than from PbS CQD bare surfaces.

The signatures of PbI_2-hybrid-amine complexes shown in CQD films are consistent with those presented in pure 2D layered perovskite films[18]. This again indicates a confined monolayer configuration for the PbI_2 matrix stabilized by the hybrid-amine ligands, consistent with conclusions drawn from absorption, PL signals and GIWAXS patterns (Fig. 2a-2d). Overall, the photophysics and crystallography studies reveal a reduction of the dimensionality during the PbI_2 crystallization process associated with the incorporation of longer amines. These open opportunities to suppress CQD fusion and the formation of thicker PbI_2 regions between CQDs. Consistent with this view, the hybrid-amine devices exhibited V_{OC} higher than the best control devices made using BTA and DMF inks (Supplementary Fig. 8).

The PbI_2-hybrid-amine matrix leads to CQD inks with improved colloidal stability (Supplementary Fig. 9) that benefit from the enhanced steric repulsion[23,24] of the longer amine surfactants (hexylamine). We also observed narrower PL peaks and higher PL quantum yields from hybrid-amine inks (Supplementary Fig. 10), indicating high-quality surfaces stabilized in the solution phase. We propose that, compared with control BTA inks, this new matrix mediates a less disruptive CQD densification process during the transition from the solution to solid phase. In this regard, *in-situ* spectroscopic ellipsometry, absorption and thermogravimetric analysis (TGA) were used to study the evolution of the CQD film thickness, absorption, and mass during post-annealing, respectively (Supplementary Fig. 11). We found that 40 - 50 % increases in film density occur, and these are associated with remarkable reductions of film thickness and the amount of volatile amine species. These changes are quantitatively much more appreciable than the near-imperceptible changes of the control BTA CQD films subjected to the same post-annealing conditions. After the post-annealing process, hybrid amine films are PV-quality films. This sol-gel-like solidification process of the PbI_2-hyrbid-amine matrix is reminiscent of sol-gel solidification processes reported in lead halide perovskites[25,26].

In the resultant CQD films, enhanced packing density and uniformity, and therefore reduced structural disorder, were also indicated in a suite of microscopic studies (Fig. 3). *Ex-situ* force-indentation curves measured with an atomic-force microscope (AFM) were used to study differences in the mechanical characteristics of CQD films stemming from different traits of the matrix materials. In agreement with observations from *in-situ* studies, the hybrid-amine films without post-annealing are characteristically soft, featuring much lower elastic moduli and larger hysteresis in the force-height response compared to control BTA films (Supplementary Fig. 12). After CQD rearrangement and densification during post-annealing, the hybrid-amine films exhibit concurrent improvements (~20%) of the elastic modulus and hysteresis compared with control BTA films (Fig. 3a and 3d). In addition, tapping-mode topographic AFM analysis of film morphology showed that the local and global smoothness can be greatly improved by using hybrid-amine inks (Fig. 3b and Supplementary Fig. 13).

For the progressively increasing field of views (5 ×5 to 30 × 30 um^2), hybrid-amine films retain a surface roughness of ~0.6 nm while control BTA films' roughness increases from 1.4 nm to ~2 nm (Fig. 3e). The enhanced elastic modulus, in conjunction with improved smoothness, implies a simultaneous optimization of CQD packing density and uniformity. Enhanced packing uniformity has recently been recognized as greatly benefitting the carrier transport in CQD assemblies[1,9,14,16,27,28].

Further analysis using grazing-incidence small-angle X-ray scattering (GISAXS) confirmed the structural enhancement both in density and uniformity[29]. The localized diffraction pattern indicates the orientational in-plane ordering of CQDs in hybrid-amine films (Fig. 3c and Supplementary 6b). This feature is absent in CQD films prepared using DMF (Supplementary Fig. 6e). Compared with control BTA films (Supplementary Fig. 10), we can clearly identify an additional ~10% densification in the planar direction and an average 6~7% densification of the inter-dot spacing from azimuthal integration[30] of the diffraction pattern (Fig. 3f). The enhanced densification is also shown in observations that hybrid-amine films produced with a post-annealing process have a narrower diffraction peak compared with control BTA films without any post-annealing. The peak is ~20 % narrower (from 0.69 nm^{-1} to 0.51 nm^{-1}), a result of the greatly enhanced packing uniformity.

The CQD packing density in the control BTA films was previously characterized as being the densest compared with other state-of-art PV-quality films (e.g., tetrabutylammonium halide salt exchanged CQD films and metal-halide perovskite exchanged CQD films)[9]. Attempts to further densify the BTA films using annealing typically deteriorated V_{OC} (Supplementary Fig. 8 and 14), a finding we attributed to the increased inhomogeneity from behavior such as CQD surface fusions[3,10,14,17]. The enhanced resistance to heterogeneous fusion during CQD densification suggests that the CQD surface is greatly preserved under the aid of PbI_2-hybrid-amine complexes.

This preservation of CQD surfaces is supported by the investigation of the energetic disordering in films (Fig. 4). As observed in photoluminescence (PL) studies (Fig. 4a), additional post-annealing

induces a visible red-shift and broadening of the peak for the best control BTA films, indicating degradation to the energetic ordering. In contrast, in the hybrid-amine films subjected to the same post-densification process, the PL features were retained (Supplementary Fig. 15) and exhibited a sharper and slightly blue-shifted PL peak relative to BTA films, corresponding to the increased energetic ordering[14,17,29]. In agreement with the above film-level studies, we also characterized the energetic disordering at the device-level by high-dynamic-range external quantum efficiency (HDR-EQE) measurements[9] in the energetic range of the bandtail (Fig. 4b). In agreement with the PL results, the bandtail of devices using hybrid-amine films is steeper than those of the best control BTA devices, and BTA films subjected to post-annealing failed to preserve the bandtail sharpness.

Encouragingly, the suppression of structural and energetic disordering in denser CQD films successfully enhances the J_{SC} and V_{OC} simultaneously in CQD PV devices (Supplementary Fig. 14), overcoming a long-lasting compromise that has been the focus of many previously attempted strategies[9–11,17].

In addition to the structural and energetic analysis, we also directly characterized the electronic parameters to quantify the enhancements to the photocarrier diffusion length for the optimized matrix. In the standard field effect transistor (FET) spectroscopy analysis[31], the hybrid-amine films exhibit higher n-type electronic mobility, associated with a sharper slope in the I_{DS}-V_{GS} response (Fig. 4c). From FET subthreshold slope state density spectroscopy (Supplementary Fig. 16), hybrid-amine films also showed a reduction in sub-bandgap state densities (6.3×10^{15} cm^{-3}) by one order of magnitude compared with the best BTA control films (5.7×10^{16} cm^{-3}).

We also conducted an analysis under contact-free and photo-activated conditions. We employed the donor-acceptor scheme[32] where a small portion of smaller-bandgap CQDs was evenly distributed in films to accept photocarriers and quench the PL emission from donor CQDs (Fig. 4d and Supplementary Fig. 17). Free charge carriers dominate the photophysical dynamics in these thick and highly-coupled

CQD films (Supplementary Fig. 18), a fact we attribute to rapid exciton dissociation.[14,33] Acceptor emission contributed from exciton diffusion and trion recombination[34,35] is negligible due to low inclusion ratio (< 0.1%) in films and low excitation intensity (<1 Sun). The PL ratio (PL emission intensity of acceptors over that of donors in a film) increases when there are more acceptors included, for a shorter diffusion distance is required for carriers to reach the acceptors. The enhancement of mobility in hybrid-amine films is quantitatively confirmed by a twofold increase in the slope of the PL ratio (Fig. 4d). We further show that, at the same time as excellent electronic transport is achieved, prolonged excited-state lifetime is observed in transient absorption (TA) measurements (Supplementary Fig. 19. See Methods). The combination of enhanced carrier transport and lifetime associated with reduced trapping defines a longer diffusion length in the hybrid-amine CQD solids.

The advantages of hybrid-amine CQD solids enable the realization of thickened PV devices that offer to enhance simultaneously J_{SC} and V_{OC}. When we increased the absorber thickness from 250 nm to 600 nm, the full spectrum external quantum efficiency (EQE) exhibits progressive broadband enhancement (Fig. 5a), with excitonic peak values of ~80% and integrated short-circuit current densities approaching 32 mA cm^{-2}, a record level in a high-efficiency CQD PV. The retained high flat response in the blue region (< 800 nm) and red excitonic region (> 900 nm) in 600 nm thick films indicates a collection efficiency free of degradation for photocarriers at both the front and rear contact, respectively. The experimentally-acquired internal quantum efficiencies (IQE) (Supplementary Fig. 20) are spectrally flat over the absorption region and indicate near-unity charge generation and collection efficiency within these thick planar devices. They rule out the energy-dependent charge generation and also argue against a strong quantitative influence of hot exciton or carrier effects.

The J_{SC} of devices with different thicknesses, measured under standard AM1.5 solar illumination conditions (Fig. 5b), agree quantitatively with the EQE measurements. No sign of J_{SC} saturation appeared when the absorber thickness was increased from 250 nm to 600 nm. In contrast, the devices using the

best-published control films showed an optimal J_{SC} (~27 mA cm^{-2}) and PCE (~11%) at the optimal thickness ~350 nm (Fig. 5c). In agreement with previous reports, control devices with thicker absorbers exhibited losses in V_{OC} (from 0.62V to 0.6V) and fill factor (FF) which we attribute to insufficient carrier diffusion lengths[9,11].

The optimal devices using hybrid-amine CQD solids (excitonic peak at ~950 nm in synthetic solution) can be achieved with thicknesses of ~500 nm. The devices showed reproducible high performance with a champion PCE = 12.48 % (Fig. 5d). One of our devices measured by an accredited PV laboratory (Newport Technology and Application Center – PV Lab) was found to display very similar figures of merit (V_{OC} = 0.647 ± 0.009 V, J_{SC} = 29.04 ± 0.60 mA cm^{-2}, FF = 63.8 ± 1.3 %) with PCE = 12.01 ± 0.26 % (Fig. 5d and Supplementary Fig. 21), the highest certified PCE reported for a CQD solar cell. This further verified the stability and reproducibility of our new strategy of matrix engineering.

We also demonstrate large-area (1.1 cm^{-2}) devices (Supplementary Fig. 22). The spatial and electrical uniformity of CQD films are verified by excellent agreement among EQE spectra measured at different locations across the large-area devices. The large-area devices exhibited Voc and Jsc values that agree well with those of small-area (0.049 cm^{-2}) devices. The somewhat lower of PCE in large-area devices relative to small-area devices majorly resides in the FF due to the limited series resistance (Rse) of the TCO (transparent conductive oxide). We believe that strategies such as integrating metal grids onto ITO can reduce the Rse limit in large-area CQD devices.

The evolution of device performance with progressively increasing matrix-to-CQD ratios (Supplementary Fig. 23) reveals the sensitivity with respect to the matrix size. The reduced Jsc×FF associated with the thicker matrix indicates the loss of inter-dot carrier hopping or tunneling. This observation supports the type-I band alignment between CQD and matrix composition in our films (Fig. 1e).

Overall, this work showcases a matrix engineering strategy that allows significant improvements of the photocarrier diffusion length in CQD solids. The enhanced structural and energetic ordering in densified CQD films allowed us to overcome the long-lasting compromise between devices' V_{OC} and J_{SC}, and therefore fulfill the advantage of building a thick device with record performance. More broadly, this study reveals the hidden sensitivity and flexibility of matrices' microscopic nature in CQD solids, and provides a means for tuning material properties within the wide-scope of CQD applications such as printable devices, tandem cells, photodetectors and LEDs.

Methods

Ligand-exchange in solution. Oleic-acid-capped PbS CQDs (bandgap ~1.3eV) dispersed in octane (50mg ml^{-1}) were used. The solution-exchange process was modified from our previous report[9]. The precursor solution for ligand exchange is made from lead halides (lead iodide 100 mM and lead bromide 40 mM) in dimethylformamide (DMF), with ammonium acetate (60 mM) to improve solubility. The ligand exchange was performed in a centrifuge tube in air. 2.5 ml PbS CQD octane solution (50mg ml^{-1}) was first diluted in 10ml octane and then added to a 20 ml precursor solution in DMF. They were mixed vigorously for ~2 mins until the CQDs totally transferred from the octane phase to the DMF phase. The CQDs in the DMF phase were washed three times using octane and then precipitated by adding toluene (50 ~ 60 % in volume ratio compared with DMF). After centrifugation, the CQDs were separated and then dried in vacuum for 30 min to get PbI_2-capped CQD solid powders.

Matrix engineering and film formation. The hybrid-amine is prepared by mixing n-butylamine (BTA), amylamine and hexylamine (volume ratio 10: 3: 2). The hybrid-amine is used to functionalize the surface of the as-prepared PbI_2-capped CQD solid powder to produce colloidal dispersions (the so-called CQD PV ink) with a large range of concentrations (170 ~ 375 mg ml^{-1}). The CQD PV inks are then spin-cast (1500 rpm for 5s and then 2000 rpm for 1min) to form initial films with different thickness. The pristine films are glassy and soft. A post-annealing at 75 ℃ for ~15 mins in an N_2-filled glovebox is performed to

solidify the matrix and densify the CQD films. In control films, BTA or DMF is used to disperse the CQD solid powder to prepare the PV ink. In best-performing BTA films, however, the post-annealing step needs to be eliminated following with previous reports. To tune the matrix-to-CQD ratio in the films, additional PbI_2 is dissolved in the solvent (hybrid-amine, BTA or DMF) to disperse CQD solid powder.

CQD planar solar cell fabrication. The ZnO nanoparticle dispersion in methanol and chloroform (1: 1 by volume ratio) is spin-cast on ITO to form an electron-transport layer (100 ~ 150 nm in thickness). The ZnO nanoparticles are synthesized following a published recipe. The CQD active absorber (250 ~ 600 nm in thickness) is deposited on the ZnO layer using the fresh PV ink following by a post-annealing step described as above. Then the hole-transport layer (~ 50 nm in thickness) is two layers of PbS CQD ligand-exchanged by 1,2-Ethanedithiol (EDT) (0.01 vol% in acetonitrile). In each layer, oleic-acid-capped CQDs (50 mg ml^{-1}) were spin-cast and followed by a 30s soaking in diluted EDT (0.01 vol% in acetonitrile) and a 3-time washing using acetonitrile. Finally, a top contact of 100 nm of gold was deposited through a shadow mask under 10^{-7} torr vacuum.

AM1.5 solar efficiency measurement. The active area (area 0.049 cm^2) is determined by the aperture placed between the solar cell and the AM1.5 solar simulator (Sciencetech class A). Through this aperture, the light intensity (1 sun, 100 mW cm^{-2}) was calibrated using a Melles–Griot broadband power meter. The spectral mismatch was calibrated using a reference solar cell (Newport). J-V curve is measured by a Keithley multimeter by scanning the bias forward (-0.7 V to 0.1 V) and backward (0.1 V to -0.7 V) to estimate the hysteresis effect. Steady-state power conversion efficiency (PCE) is then measured by fixing the bias at the maximum power output point (V_{MPP}) determined from J-V curves (Supplementary Fig. 24).

Rutherford backscattering spectroscopy (RBS). RBS measurements were performed at the Tandetron facility at the University of Western Ontario. CQD films of ~300 nm thickness were deposited on Si substrates to avoid overlaps with the main elements in CQD films. All samples were measured with a 3.7 MeV He++ beam (non-Rutherford resonance for nitrogen) and a dose of 10 μC.

Grazing-incidence small-angle and wide-angle X-ray spectroscopy (GISAXS and GIWAXS). GISAXS was carried out at the Cornell High Energy Synchrotron Source (CHESS). The wavelength of the X-ray beam was 1.17 Å. A wide band-pass (1.47 %) double-bounce multilayer monochromator was employed. Incident angle was set to 0.5° with respect to the sample plane. The exposure time was 3 seconds. GISAXS and GIWAXS were also conducted using a SAXSLab Ganesha at the South Carolina SAXS Collaborative. A Xenocs GeniX 3D microfocus source was used with a copper target to produce monochromatic beam with a 0.154 nm wavelength. The instrument was calibrated just prior to measurement, using National Instrument of Standard and Technology (NIST) reference material 640c. A Pilatus 300k detector (Dectris) was used to collect the two-dimensional (2D) scattering pattern with nominal pixel dimension of 172x172 μm. GISAXS data were acquired with an incident X-ray angle (α_i) of 0.5^o with respect to the substrate using an X-ray flux of ~21.4M photons per second upon the samples. Likewise, GIWAXS data were collected with α_i=2° and an X-ray flux of ~36.3M photon per second. The sample-to-detector distance was maintained at 452.1 or 112.1 mm for GISAXS and GIWAXS measurements, respectively.

Long-time transient absorption (Flash Photolysis). Pump pulses were generated with a regenerative amplified Yb:KGW laser at a 5 kHz repetition rate (PHAROS, Light Conversion). The 1030 nm fundamental was sent through an optical parametric amplifier (Light Conversion, Orpheus), and the second harmonic of the idler was chosen for the 750 nm pump pulse. The probe was generated by a CW 1310 nm laser diode (Newport, LPM1310-05E). Both beams were focused onto the sample, and the probe was coupled to an InGaAs amplified Detector (Thorlabs, PDA10D). The lifetime response was measured using a 1 GHz oscilloscope (Agilent, DSO8104A), which was triggered by the pump laser.

Atomic force microscopy (AFM). AFM study was done with an Asylum Research Cypher AFM equipped with AC240TM-R3 probes (resonant frequency 70 kHz, spring constant 2 N/m).

Nanomechanical force spectroscopy was conducted with a trigger indentation force of 8 nN loaded at a rate of 2 μm/s. Topographic imaging was performed in tapping-mode.

Other characterizations

Fourier transform infrared spectroscopy (FTIR) measurements are done using a Bruker Vertex 80 (4000 to 600 cm^{-1}; resolution 4 cm^{-1}) in top-configuration (attenuated total reflection, ATR). **Steady-state photoluminescence (PL)** was carried out using an HORIBA Fluorolog-3 Spectrofluorometer equipped with UV/VIS/NIR photomultiplier tube detectors and a monochromatized Xenon lamp excitation. **UV-Vis-IR absorption** was carried out on a PerkinElmer LAMBDA 950 Spectrophotometer. **External-quantum-efficiency (EQE)** spectrum measurements were carried out following a previously published processes[4].

Data availability

The authors declare that the data supporting the findings of this study are available within the paper and its supplementary information files. The data that support the findings of this study are available from the corresponding authors upon reasonable request.

Acknowledgements

This publication is based in part on work supported by the Natural Sciences and Engineering Research Council (NSERC) of Canada, by the Ontario Research Fund Research Excellence Program, and by the Award OSR-2017-CPF-3321-03, made by King Abdullah University of Science and Technology (KAUST). We thank U-ser Jeng for GIWAXS data tested at the National Synchrotron Radiation Research Center, Taiwan, Republic of China. This work made use of the South Carolina SAXS Collaborative using a SAXSLab Ganesha, supported by the NSF Major Research Instrumentation program (award #DMR-1428620). We thank L. Goncharova for assistance with RBS measurements. We thank D. Kopilovic, E.

Palmiano, L. Levina and R. Wolowiec for the technical support. M.L. acknowledges support from the Project of Innovation-Driven Plan in Central South University (2017CX003), Project from State Key Laboratory of Powder Metallurgy in Central South University, Thousand Youth Talents Plan of China and Hundred Youth Talents Program of Hunan.

Author contributions

J.X. conceived the idea and contributed to most experimental work. E.H.S. supervised the project. O.V., A.A., and S.O.K. co-supervised the project. M.L. assisted in device fabrication and experiment design. S.H. assisted in devices certificate and experiment design. A.R.K., M. A. and A.A. performed the in-situ measurements of film formation. R.M., M.S., A.S., and R.Q.B. carried out GISAXS/WAXS measurements. G.W. and M.W. performed AFM and PL measurements. A.P. performed TA measurements. B.S. carried out FET measurements. O.V. and O.O carried out the device simulations. M.L. carried out microscopic studies. O.V. facilitated RBS analysis. J.X., O.V. and E.H.S. wrote the manuscript. All the authors assisted in experiments and provided comments on the text.

Competing financial interests

The authors declare no competing financial interests.

Additional information

Supplementary information is available in the online version of the paper. Reprints and permission information is available online at www.nature.com/reprints. Correspondence and requests for materials should be addressed to Edward H. Sargent.

References

1. Kagan, C. R., Lifshitz, E., Sargent, E. H. & Talapin, D. V. Building devices from colloidal quantum dots. *Science* **353,** aac5523 (2016).
2. Luther, J. M. *et al.* Schottky Solar Cells Based on Colloidal Nanocrystal Films. *Nano Lett.* **8,** 3488–3492 (2008).
3. Ip, A. H. *et al.* Infrared Colloidal Quantum Dot Photovoltaics via Coupling Enhancement and Agglomeration Suppression. *ACS Nano* **9,** 8833–8842 (2015).
4. Ip, A. H. *et al.* Hybrid passivated colloidal quantum dot solids. *Nat. Nanotechnol.* **7,** 577–582 (2012).
5. Tang, J. *et al.* Colloidal-quantum-dot photovoltaics using atomic-ligand passivation. *Nat. Mater.* **10,** 765–771 (2011).
6. Ning, Z. *et al.* Air-stable n-type colloidal quantum dot solids. *Nat. Mater.* **13,** 822–828 (2014).
7. Dirin, D. N. *et al.* Lead Halide Perovskites and Other Metal Halide Complexes As Inorganic Capping Ligands for Colloidal Nanocrystals. *J. Am. Chem. Soc.* **136,** 6550–6553 (2014).
8. Chuang, C.-H. M., Brown, P. R., Bulović, V. & Bawendi, M. G. Improved performance and stability in quantum dot solar cells through band alignment engineering. *Nat. Mater.* **13,** 796–801 (2014).
9. Liu, M. *et al.* Hybrid organic-inorganic inks flatten the energy landscape in colloidal quantum dot solids. *Nat. Mater.* **16,** 258–263 (2016).
10. Carey, G. H., Levina, L., Comin, R., Voznyy, O. & Sargent, E. H. Record Charge Carrier Diffusion Length in Colloidal Quantum Dot Solids via Mutual Dot-To-Dot Surface Passivation. *Adv. Mater.* **27,** 3325–3330 (2015).
11. Lan, X. *et al.* 10.6% Certified Colloidal Quantum Dot Solar Cells via Solvent-Polarity-Engineered Halide Passivation. *Nano Lett.* **16,** 4630–4634 (2016).
12. Dolzhnikov, D. S. *et al.* Composition-matched molecular 'solders' for semiconductors. *Science* **347,** 425–428 (2015).
13. Ning, Z. *et al.* Quantum-dot-in-perovskite solids. *Nature* **523,** 324–328 (2015).

14. Gilmore, R. H., Lee, E. M. Y., Weidman, M. C., Willard, A. P. & Tisdale, W. A. Charge Carrier Hopping Dynamics in Homogeneously Broadened PbS Quantum Dot Solids. *Nano Lett.* **17,** 893–901 (2017).

15. Guyot-Sionnest, P. Electrical Transport in Colloidal Quantum Dot Films. *J. Phys. Chem. Lett.* **3,** 1169–1175 (2012).

16. Akselrod, G. M. *et al.* Visualization of exciton transport in ordered and disordered molecular solids. *Nat. Commun.* **5,** ncomms4646 (2014).

17. Chuang, C.-H. M. *et al.* Open-Circuit Voltage Deficit, Radiative Sub-Bandgap States, and Prospects in Quantum Dot Solar Cells. *Nano Lett.* **15,** 3286–3294 (2015).

18. Blancon, J.-C. *et al.* Extremely efficient internal exciton dissociation through edge states in layered 2D perovskites. *Science* eaal4211 (2017). doi:10.1126/science.aal4211

19. Congreve, D. N. *et al.* Tunable Light-Emitting Diodes Utilizing Quantum-Confined Layered Perovskite Emitters. *ACS Photonics* **4,** 476–481 (2017).

20. Zhang, J. *et al.* Layered ultrathin PbI2 single crystals for high sensitivity flexible photodetectors. *J. Mater. Chem. C* **3,** 4402–4406 (2015).

21. Derenzo, S. E. *et al.* Experimental and theoretical studies of donor–acceptor scintillation from PbI2. *J. Lumin.* **134,** 28–34 (2013).

22. Cooper, J. K., Franco, A. M., Gul, S., Corrado, C. & Zhang, J. Z. Characterization of Primary Amine Capped CdSe, ZnSe, and ZnS Quantum Dots by FT-IR: Determination of Surface Bonding Interaction and Identification of Selective Desorption. *Langmuir* **27,** 8486–8493 (2011).

23. Sayevich, V. *et al.* Hybrid N-Butylamine-Based Ligands for Switching the Colloidal Solubility and Regimentation of Inorganic-Capped Nanocrystals. *ACS Nano* (2017). doi:10.1021/acsnano.6b06996

24. Anderson, N. C., Hendricks, M. P., Choi, J. J. & Owen, J. S. Ligand Exchange and the Stoichiometry of Metal Chalcogenide Nanocrystals: Spectroscopic Observation of Facile Metal-Carboxylate Displacement and Binding. *J. Am. Chem. Soc.* **135,** 18536–18548 (2013).

25. Barrit, D. *et al.* Hybrid perovskite solar cells: In situ investigation of solution-processed PbI2 reveals metastable precursors and a pathway to producing porous thin films. *J. Mater. Res.* **32,** 1899–1907 (2017).

26. Munir, R. *et al.* Hybrid Perovskite Thin-Film Photovoltaics: In Situ Diagnostics and Importance of the Precursor Solvate Phases. *Adv. Mater.* **29,** 1604113 (2017).

27. Akselrod, G. M. *et al.* Subdiffusive Exciton Transport in Quantum Dot Solids. *Nano Lett.* **14,** 3556–3562 (2014).

28. Sandeep, C. S. S. *et al.* Epitaxially Connected PbSe Quantum-Dot Films: Controlled Neck Formation and Optoelectronic Properties. *ACS Nano* **8,** 11499–11511 (2014).

29. Murray, C. B., Kagan, and C. R. & Bawendi, M. G. Synthesis and Characterization of Monodisperse Nanocrystals and Close-Packed Nanocrystal Assemblies. *Annu. Rev. Mater. Sci.* **30,** 545–610 (2000).

30. Hanrath, T., Choi, J. J. & Smilgies, D.-M. Structure/processing relationships of highly ordered lead salt nanocrystal superlattices. *ACS Nano* **3,** 2975–2988 (2009).

31. Rolland, A., Richard, J., Kleider, J. P. & Mencaraglia, D. Electrical Properties of Amorphous Silicon Transistors and MIS- Devices: Comparative Study of Top Nitride and Bottom Nitride Configurations. *J. Electrochem. Soc.* **140,** 3679–3683 (1993).

32. Zhitomirsky, D., Voznyy, O., Hoogland, S. & Sargent, E. H. Measuring Charge Carrier Diffusion in Coupled Colloidal Quantum Dot Solids. *ACS Nano* **7,** 5282–5290 (2013).

33. Choi, J. J. *et al.* Photogenerated Exciton Dissociation in Highly Coupled Lead Salt Nanocrystal Assemblies. *Nano Lett.* **10,** 1805–1811 (2010).

34. Makarov, N. S. *et al.* Spectral and Dynamical Properties of Single Excitons, Biexcitons, and Trions in Cesium–Lead-Halide Perovskite Quantum Dots. *Nano Lett.* **16,** 2349–2362 (2016).

35. Park, Y.-S., Bae, W. K., Pietryga, J. M. & Klimov, V. I. Auger Recombination of Biexcitons and Negative and Positive Trions in Individual Quantum Dots. *ACS Nano* **8,** 7288–7296 (2014).

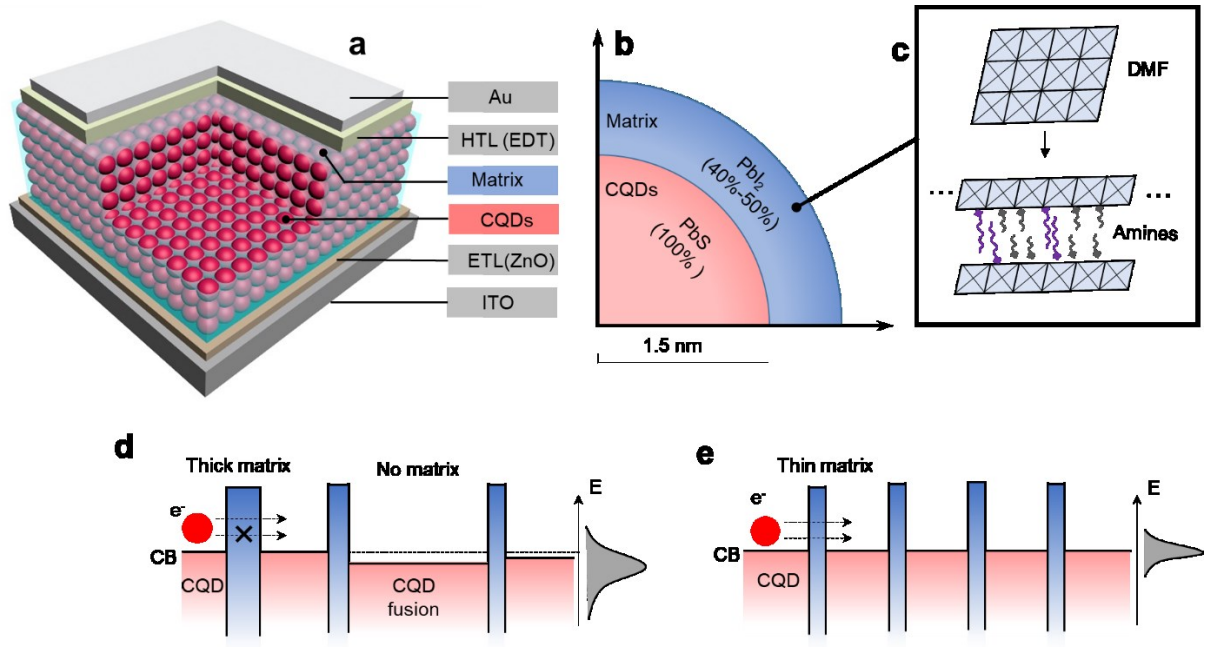

Figure 1 | Engineering the microscopic nature of the matrix to increase ordering and the photocarrier-diffusion-length in CQD solids for solar cells. **a**, Schematic diagram of the effective medium model of the CQD absorber in a solar cell, where CQDs (red) assemble in a matrix medium (blue). **b**, In published best-performing PbS CQD PV solids, the matrix component is PbI_2 and its amount is 40 ~50 % compared with PbS in molecular ratio, enough to account for the formation of a full monolayer coverage on the surfaces of the PbS CQDs (bandgap ~1.3 eV and diameter ~3 nm). **c,** Dimethylformamide (DMF) and hybrid amines are used to functionalize the PbI_2 matrix component and tailor the matrix's microstructure and distribution during its reorganization that occurs when the CQDs are solidified from solution. The PbI_2-hybrid amine coordinating complex has a self-confined 2D layered structure that greatly suppresses inhomogeneity of the matrix due to random 3D growth in DMF. **d,** Inhomogeneity of the matrix increases the structural and energetic disorder and reduces the diffusion length and open-circuit voltage (V_{OC}). CQD over-isolation due to local matrix agglomeration will block carrier transport. CQD over-coupling due to surface fusion caused by the absence of matrix tends to increase the V_{OC} deficit. **e,** Confining the matrix dimensionality between CQDs and improving its homogeneity throughout the film increases the photocarrier diffusion length and reduces the V_{OC} deficit.

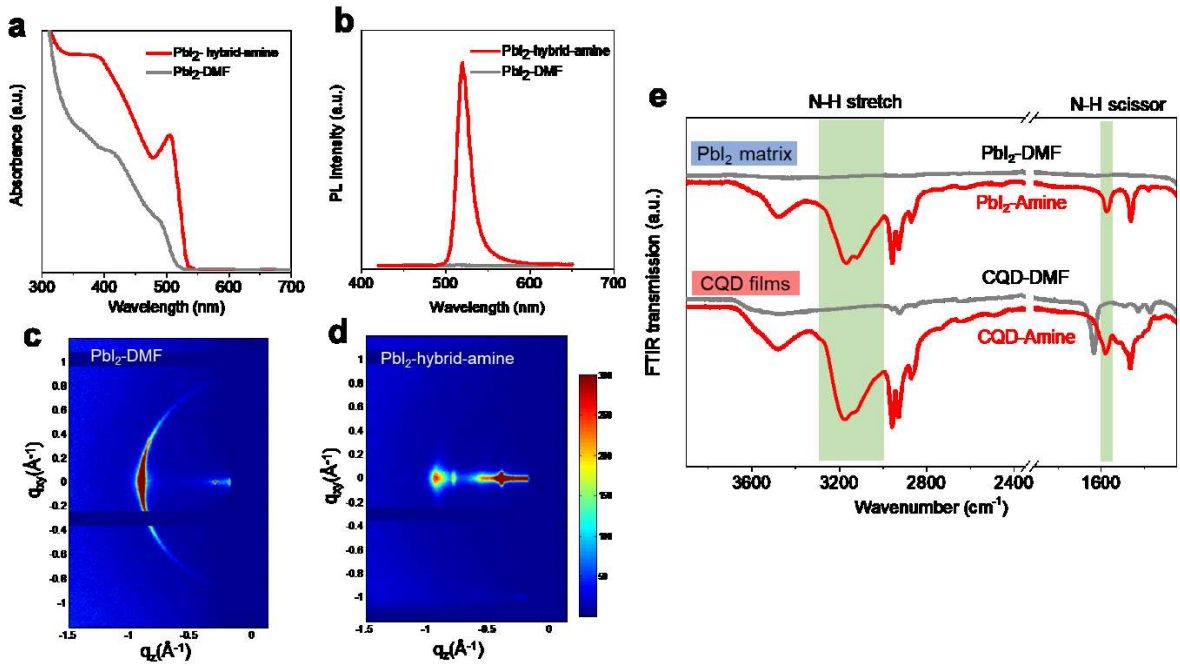

Figure 2 | Enhanced 2D confinement in the matrix of CQD solids. **a**, UV-visible-NIR absorption curves of PbI_2 deposited from hybrid amines (red) and dimethylformamide (DMF, dark grey). Hybrid amine films show the strong excitonic feature located at the bandedge (~500 nm), resulting from the quantum confinement effect in layered configurations of PbI_2-hybrid-amine coordinating complexes. DMF films show no excitonic feature. **b**, Room-temperature photoluminescence (PL) of PbI_2 deposited from hybrid amines and DMF (dark grey), compared with reference PL of 2D layered perovskite single crystal (black) and 2D perovskite film (dash). Hybrid amine films show a narrow and asymmetric PL peak. DMF films show no PL features. **c**, **d,** GIWAXS patterns for (**c**) PbI_2 deposited from DMF and (**d**) PbI_2 deposited from hybrid amines. PbI_2-hybrid-amine complex shows a near-single-crystalline pattern of 2D monolayer structure in parallel with the substrate. **e**, Attenuated total reflection fourier transform infrared spectroscopy (ATR-FTIR) of PbI_2-amine coordinating complex signatures in N-H stretch modes (green band at ~3200 cm^{-1}) and N-H scissor modes (green band at ~1590 cm^{-1}). PbI_2 films and CQD films deposited using hybrid amines (red) show consistent signatures of PbI_2-amine coordinating complexes. PbI_2 films and CQD films deposited using DMF (grey) show no signatures of PbI_2-amine coordinating complexes.

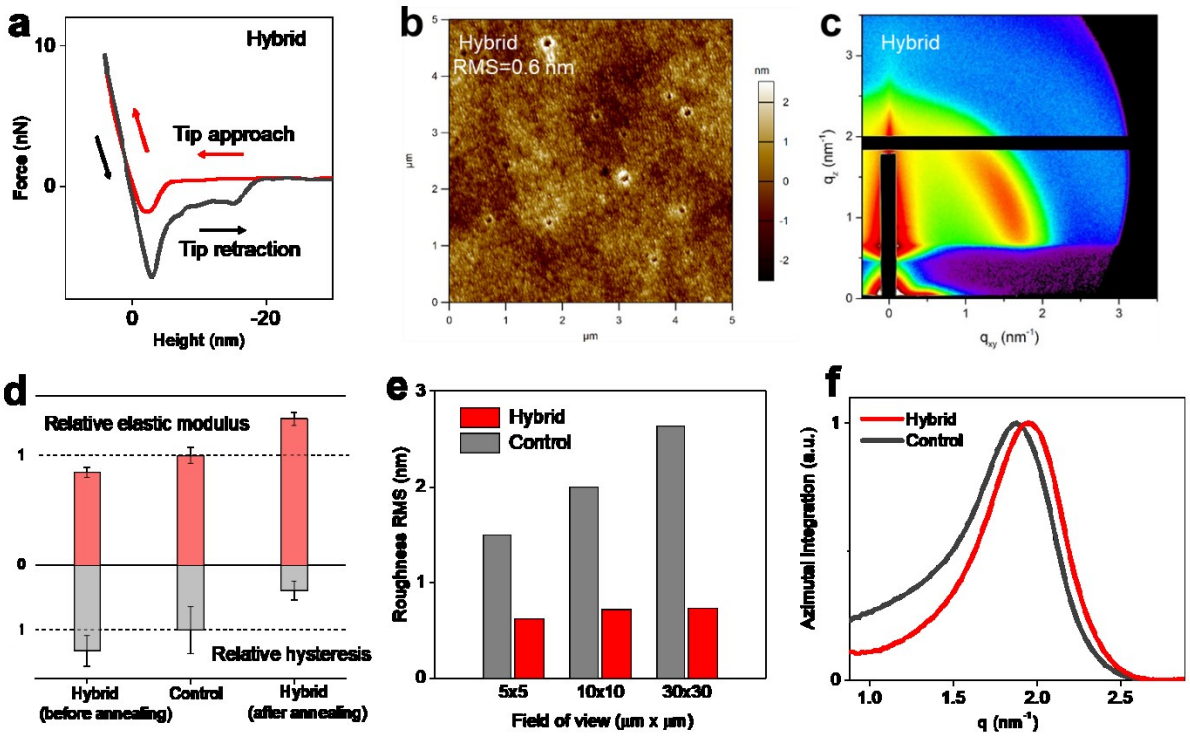

Figure 3 | Enhanced packing density and uniformity, and reduced structural disorder in CQD solids for solar cells. **a**, Mechanical characteristics of hybrid amine films (force-indentation curves) measured by an atomic-force microscope (AFM). Arrows indicate the tip approach and retraction. **d**, Elastic moduli and plastic deformation (calculated from the slope and its hysteresis in the linear rising region of force-indentation curves) between hybrid amine films (before and after post-annealing) and best-performing control films. Post-annealed hybrid amine films are PV-quality films and are characterized in the following panels (c, d, e and f). **b**, Topographic AFM morphology analysis of hybrid amine films, showing surface roughness ~0.6 nm. **e**, Over progressively increasing the field of views (5 ×5 to 30 × 30 um^2), hybrid amine films (red) exhibit greatly reduced roughness compared with best control films (grey). **c**, The GISAXS two-dimensional pattern of the hybrid amine films. The vertical black line on the left corner is the beam stop and the horizontal black line is due to the Pilatus 200k detector. The localized diffraction peak indicates the orientational in-plane ordering of the CQD assembly. **f**, Azimuthally integrated intensities of the diffraction peak. They show the distribution of inter-dot *d*-spacing (*d*~1/q) in the CQD assembly. The hybrid films (red) exhibit ~10 % reduced in-planar *d*-spacings, ~7 % reduced directional-average *d*-spacings and ~20 % narrower peaks, compared with control films (grey), suggesting the concurrently enhanced packing density and homogeneity of CQDs.

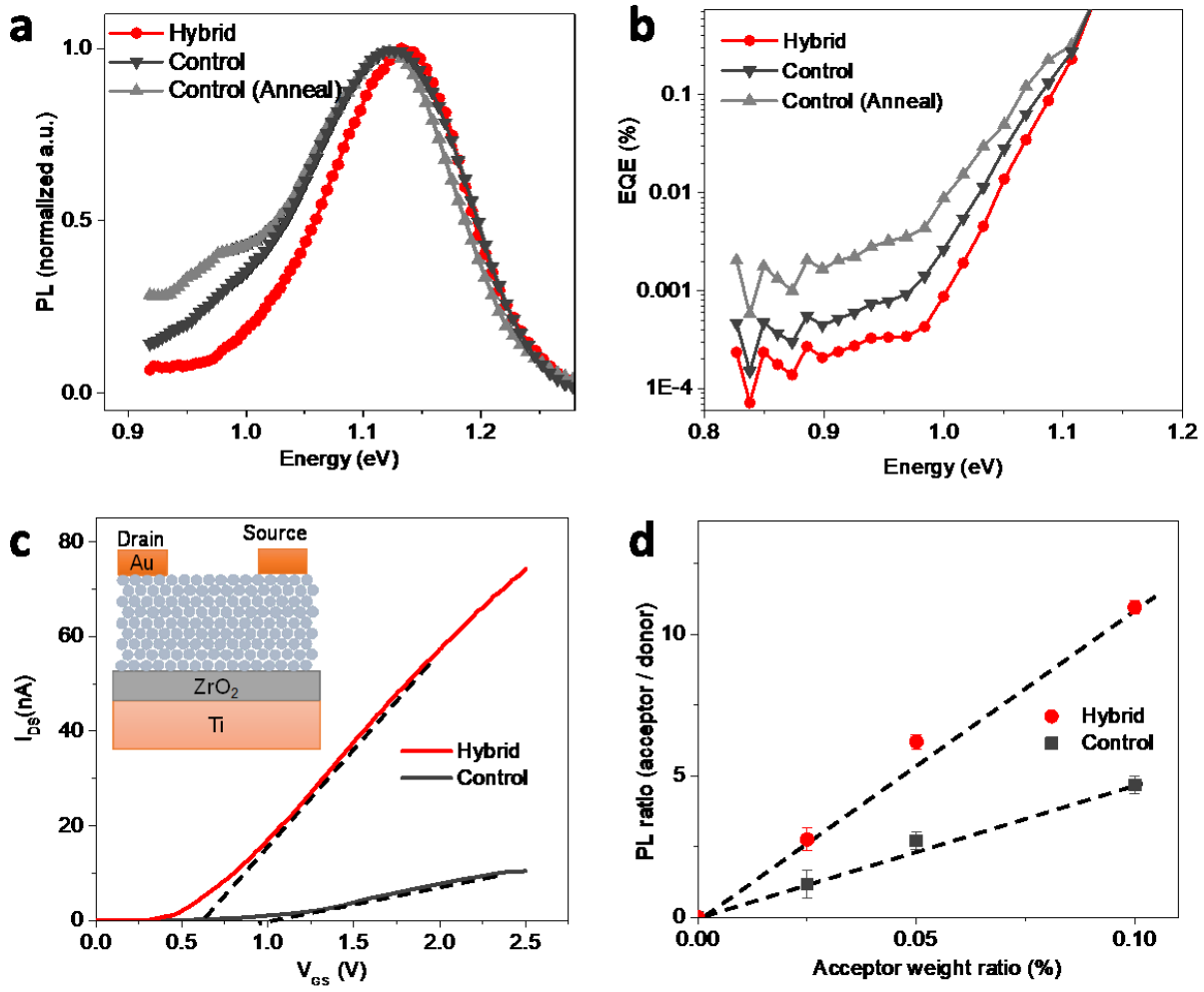

Figure 4 | Reduced energetic disorder and enhanced electronic transport in CQD solids. **a**, The photoluminescence (PL) of hybrid amine films (red, circle) is sharper and slightly bluer than best-performing control films (dark grey, down-pointing triangle). Control films densified via a post-annealing process, the same as that used in hybrid amine films, exhibit lower-energy and broader PL (light grey, up-pointing triangle) than control films. **b**, The high dynamic range external-quantum-efficiency (HDR-EQE) of devices using hybrid amine solids (red, circle) is sharpest compared with best-performing control devices (dark grey, down-pointing triangle) and devices using annealed control films (light grey, up-pointing triangle), representing reduced concentrations and depths of bandtail states. **c**, Transfer characteristics of FETs using control and hybrid amine CQD films (red) and best-performing control CQD films (dark grey). The sharper slope of the I-V curve indicates a higher electronic mobility. Inset of c shows the FET device structure. **d**, Transfer characteristics of photo-actived carriers in donor-acceptor films using hybrid amine CQDs (red) and control CQDs (dark grey). A sharper slope in the PL ratio (acceptor over the donor) curve indicates a higher mobility and longer diffusion length for photocarriers. Inset of d shows the photocarrier dynamics in donor-acceptor films.

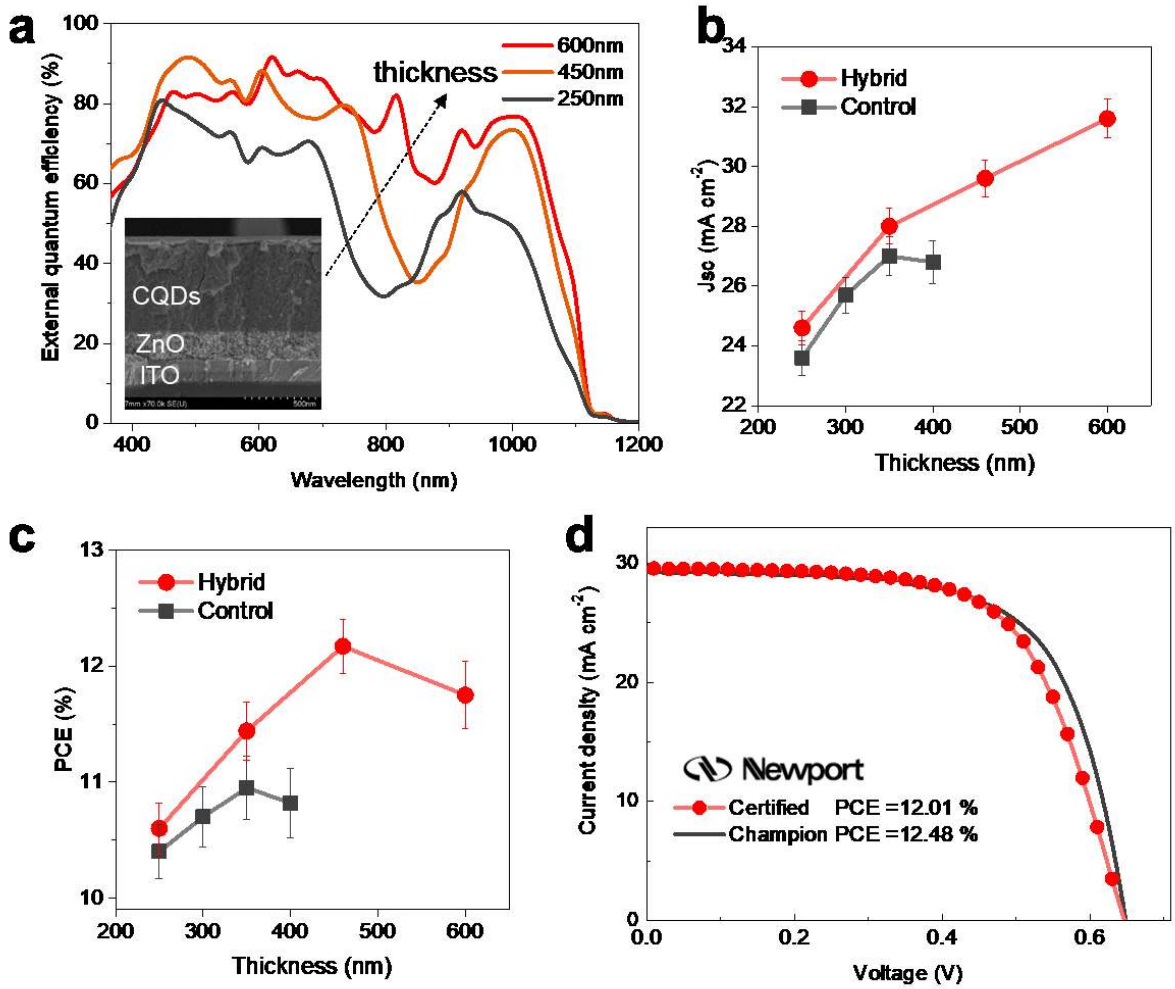

Figure 5 | Enhanced solar cell performance in thick CQD absorbers resulting from increased photocarrier diffusion lengths. **a**, The full spectrum external-quantum-efficiency (EQE) increased continuously when the thickness of the absorber, prepared from a hybrid amine ink, is increased from 250 nm to 600 nm. Inset, the cross-sectional SEM image of a representative device structure. **b**, The comparison of J_{SC} dependence on absorber thickness between hybrid amine (red curve) and best-performing control devices (control, grey curve). J_{SC} in control devices saturates when the thickness exceeds 350 nm. J_{SC} in hybrid amine devices keeps rising when thickness reaches 600 nm. The devices are tested under AM1.5 100 mW cm^{-2} illumination conditions. **c**, The comparison of absorber-thickness-dependent PCE between different types of devices. The optimal thickness of the best control devices (grey curve) is ~350 nm. The optimal thickness of hybrid amine devices (red curve) is in the range of ~500 nm. The champion PCE of the hybrid amine device is 12.48 %. **d**, J-V curve of a certified device exhibiting a PCE of 12.01 %, the highest ever reported. Statistics for each type of device is calculated using 12 samples fabricated in the same batch.